High Resolution Imaging Camera (HiRIC) on China's First Mars Exploration Tianwen-1 Mission

Qingyu Meng[1] · Dong Wang[1] · Xiaodong Wang[1] · Wei Li[1] · Xianwei Yang[1] · Dejie Yan[1] ·
Yang Li[1] · Zhirui Cao[1] · Qi Ji[1] · Tianyu Sun[1] · Wei Yan[2] · Kejun Wang[1] · Xiaobo Li[1] ·
Jingtao Huang[1] · Zheng Wang[1] · Weiguo Zhao[1] · Yan Wang[1] · Yunfeng He[1] ·
Xianpeng Hao[1] · Wenguang Liu[1] · Bowei Zhang[1] · Pengji Zhou[1] · Yunhui Li[1] ·
Haibo Zhao[1] · Lin Lu[1] · Hainan Guan[1] · Dali Zhou[1] · Fanlu Wu[1,2] · Fan Zhang[1] ·
Shiyu Zhu[3] · Jihong Dong[1]

Abstract

The High-Resolution Imaging Camera (HiRIC) is one major payload of China's first Mars exploration mission, and its main objective is to obtain the detailed observation images of the key areas on the Martian surface. In this paper, the leading group of HiRIC shows a full blueprint of the HiRIC. The HiRIC can achieve a high resolution (0.5 m at an altitude of 265 km) with a wide swath width of 9 km. The HiRIC adopts an Off-Axis Three-Mirror Astigmatic (TMA) optical system with a focal length of 4640 mm, an F-number of 12 and a Field of View (FOV) of $2° \times 0.693°$. In order to reduce the instrument weight, carbon-based material is widely used in the opto-mechanical structure which is in ultra-lightweight design, thus, a light-weight camera with a total mass of 42 kg is obtained. The Time Delay and Integration (TDI) Charge Coupled Devices (CCDs) and Complementary Metal-Oxide-Semiconductor Transistor (CMOS) detectors are all set on the imaging plane to achieve the push-broom imaging and frame imaging, respectively. And the high Signal-to-Noise Ratio (SNR) >100:1 can achieve in multi observation types for various scientific imaging tasks. After 4-year design and fabricate, the HiRIC has been assembly. The testing results show that the instrument is in good condition, and the Modulation Transfer Function (MTF) can achieve 0.18 at Nyquist frequency. The HiRIC can achieve a well image on China first Mars exploration mission.

✉ W. Yan
  yanw@nao.cas.cn

✉ J. Dong
  dongjihong@ciomp.ac.cn

[1] Changchun Institute of Optics, Fine Mechanics and Physics, Chinese Academy of Sciences, Changchun 130033, China

[2] Key Laboratory of Lunar and Deep Space Exploration, National Astronomical Observatories, Chinese Academy of Sciences, Beijing 100101, China

[3] Changchun UP Optotech (Holding) Co., Ltd., Changchun 130033, China

1 Introduction

In 2016, China officially announced the China's first Mars exploration mission (Tianwen-1) that seeks to understand whether Mars was, is, or will possibly be, a habitable planet, and how geologic, climatic, and other processes have worked to shape Mars and its environment over time, as well as how they interact today. After four years' efforts, China's first Mars exploration probe been successfully launched in 2020. China's first Mars mission can be divided into 6 stages, including launch, Earth-Mars transfer, Mars capture, Mars parking, EDL (Entry, Descent, Landing) and scientific exploration. After successfully launching and traveling for 6 and a half months in the Earth-Mars transfer orbit, the probe will be captured by the Mars and enter an elliptical orbit around the Mars with a period of 10 sols. After orbit maneuver at the apoareon, the probe will be adjusted to a circumpolar orbit and then enter the Mars parking orbit with a period of about 2 days by three times of periareon braking. Two to three months later, the rover will be released by the orbiter and landed on the Martian surface to start its patrolling detection. After releasing of the rover, the orbiter will perform orbit maneuver and enter the relay orbit with a period of about 8.2 hours, communicate with the rover and start its scientific exploration. 90 sols later, remote sensing orbit stage will start after orbit adjustment and last for one Martian year. The remote sensing orbit is a large ellipse with the altitudes of periareon and apoareon about 265 km and 11900 km, respectively. The orbit inclination is $90° \pm 5°$, and the orbital period is 7.8 hours.

High-Resolution Imaging Camera (HiRIC) will be loaded on Tianwen-1 probe to acquire detailed images of the key areas on Martian surface. As the leading group of HiRIC, we have developed a 0.5 m resolution camera for observing the formation and dynamic changes of Martian geological phenomena, and also providing scientific data to identify the suitable landing site. The high-resolution images can characterize in detail the stratigraphy, geologic structure and composition of the Martian surface. Here in this paper, we disclosed for the first time the full picture/technical scheme of HiRIC, including its objectives, optical, mechanical, electrical and thermal design, its instrument test, calibration and performance overview, its working mode and observation target.

2 Overview and Objectives of HiRIC

2.1 Scientific Objectives

For the purpose of the Mars landing survey, Martian global and comprehensive exploration, and detailed inspections of key areas on the surface in one single mission, Tianwen-1 is consisted of an orbiter and a landing rover. One of the major missions for the orbiter is to conduct the real-time sensitive global remote sensing of Mars, which can be used to study the dynamics of the Mars' topography and help to determine the landing site. As we know, the orbiter flies around Mars in a large elliptical orbit, and its altitude is constantly changing. Therefore, a common medium resolution camera would not satisfy all the needs of researchers and a highly accurate HiRIC is needed on the orbiter.

In our developed HiRIC, time-sensitive and true-color images with a highest resolution of 0.5 m (at an altitude of 265 km) and different coverage widths can be obtained at different altitudes. With the HiRIC, we can obtain detailed observation images of the key areas on the Martian surface. The objectives of the HiRIC are listed including detailed observation of key areas on the Martian surface, periodic revisit observation of key areas on the Martian

surface, high-resolution observations of the landing area, dynamic observations of weather phenomena on Mars.

2.2 Instrument Performance

According to the objectives of the HiRIC, the main technical targets of the HiRIC are analyzed and determined, including the ground pixel resolution, the ground swath width, the working spectrum.

2.2.1 Ground Pixel Resolution

The ground pixel resolution of the HiRIC is 0.5 m, which guarantees the detailed observation of the Martian surface rocks, the sufficient analysis of the geological evolution of Mars and determining the optimal landing sites for the rovers.

2.2.2 Ground Swath Width

At the perigee of the Mars, the ground swath width of the HiRIC is about 9 km; the corresponding FOV angle is ∼2°. The three-axis pointing accuracy of the orbiter is about ± 0.5°, and even if the three-axis pointing changes, the HiRIC can still obtain high-resolution images of the observation target.

2.2.3 Working Spectrum

The energy at the entrance pupil of the camera will be improved, and the signal to noise ratio of the camera will be improved if the working spectrum segment with high ground albedo is chosen. Ferriferous is the most widely distributed mineral detected on Mars. Phyllosilicates, sulfates, olivine and other minerals are also found in related regions on Mars. These typical Martian minerals have a high reflectivity in the visible light range of 0.5 μm to 0.8 μm, which is the reason for the orange-red appearance of Mars (Murchie et al. 2007). The HiRIC is designed by the 8.75 μm, 6144 pixels TDI CCD with a maximum of 96 integral stages to meet the requirements of mission objectives and system. The same type of device has been used in many of our aerospace products. The response band of this TDI CCD is 0.45 μm∼0.9 μm, which can cover the demand range of scientific targets.

3 Instrument Design

From the perspective of engineering design, the HiRIC consists of optical subsystem, Optomechanical structure subsystem, electronics subsystem, thermal control subsystem, and so on. In order to accomplish the planned scientific objectives, the HiRIC needs to have sufficient performance. But at the same time, in order to reduce the carrying burden of the satellite platform, the weight of the HiRIC is controlled at less than 43 kg, which puts extremely strict requirements on the engineering design of the camera. The design scheme of HiRIC will be introduced below from each sub-system branch.

3.1 Optics

3.1.1 Optical System Design

The HiRIC optical system has a focal length of 4640 mm, a field of view (FOV) of 2° × 0.693° and an F-number of 12. Benefit from the advantages of wide FOV and non-obscuration for off-axis unobstructed optical system, which makes a better spot diagram
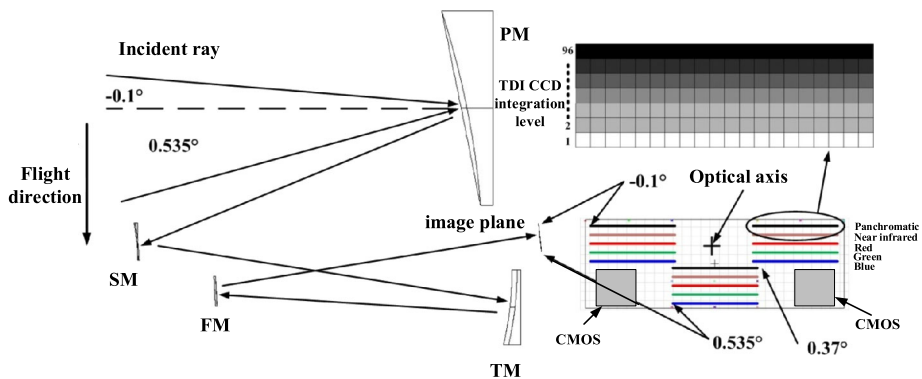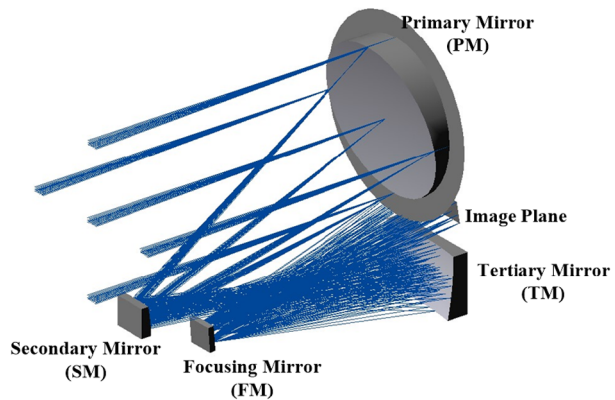
Fig. 1 Optical system

Fig. 2 Schematic diagram of imaging relationship

energy concentration and improved observation frequency of specified target areas (Meng et al. 2018), the HiRIC adopts a Relayed COOK off-axis three-mirror anastigmatic (TMA) optical system, shown in Fig. 1.

The optical system has a larger telephoto ratio. Compared to the system focal length of 4640 mm, the distance between the primary mirror (PM) and secondary mirror (SM) is just 723 mm, and the distance between the SM and TM is 800.000 mm.

In the HiRIC off-axis TMA optical system, the PM aperture size is Φ387 mm, the SM aperture size is 89 mm × 74.5 mm, and the tertiary mirror (TM) aperture size is 243 mm × 155.5 mm. In order to be able to adapt to the impact of the carrying conditions, space environment and orbital height change on the imaging quality of the HiRIC, the optical system set a plane mirror as the focusing mirror (FM) with an aperture size of 68 mm × 63 mm.

There are three TDICCD detectors and two area array CMOS detectors on the image plane. The schematic diagram of imaging relationship is shown in Fig. 2. In the optical system coordinate system, the FOV of −0.1° in the tangential direction corresponds to the panchromatic imaging area of the TDI CCD, and the FOV of +0.535° in the tangential direction corresponds to the blue imaging area of the TDI CCD. The FOV range is from −1.0° to +1.0° in the sagittal direction. Mapping to the optical system coordinate system,
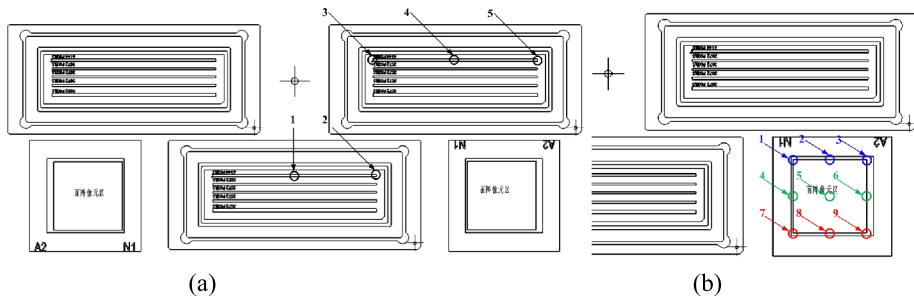
Fig. 3 Characteristic field points on the detectors for the optical system layout. (**a**) Global graph; (**b**) CMOS area enlarged view

Table 1 The MTF design value of the panchromatic TDI CCD field range of characteristic field points (λ: 450 nm∼900 nm)

Field number	Tangential (57 lp/mm)	Sagittal (57 lp/mm)	Average value
1	0.425	0.432	0.429
2	0.414	0.417	0.416
3	0.42	0.425	0.423
4	0.424	0.421	0.423
5	0.421	0.422	0.422
Average value	0.421	0.423	0.422

Table 2 The MTF design value of the CMOS field range of characteristic field points (λ: 450 nm∼900 nm)

Field number	Tangential (45 lp/mm)	Sagittal (45 lp/mm)	Average value
1	0.526	0.533	0.5295
2	0.514	0.534	0.524
3	0.455	0.526	0.4905
4	0.518	0.53	0.524
5	0.484	0.54	0.512
6	0.385	0.517	0.451
7	0.5	0.526	0.513
8	0.431	0.534	0.4825
9	0.282	0.5	0.391
Average value	0.455	0.527	0.491

the satellite flight direction is from the FOV of −0.1° to +0.535°, and the TDI CCD integral direction is from the blue imaging area to the panchromatic imaging area.

The optical image quality is symmetrical. The characteristic field points of the TDI CCD panchromatic segment are points 1-5, as shown in Fig. 3(a); and the characteristic field points of the CMOS area array detector are points 1-9, as shown in Fig. 3(b). The imaging quality(MTF)is shown in Table 1 and Table 2. The TDI CCD pixel size is 8.75 μm, and the Nyquist frequency is 57 line pairs per millimeter, and the CMOS pixel size is 11 μm, and
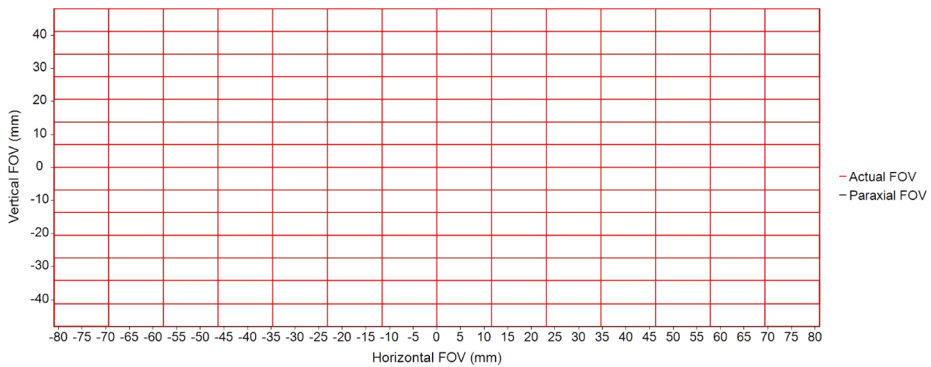
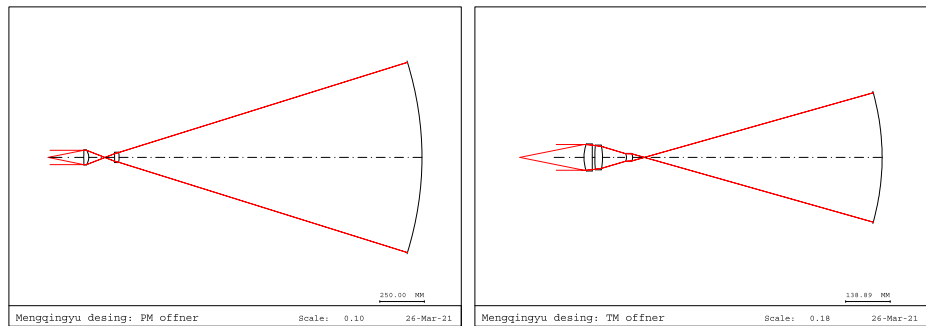**Fig. 4** The grid distortion of the optical system

Fig. 5 The PM and TM testing optical path design

the Nyquist frequency is 45 line pairs per millimeter. In the Table 1 and Table 2, the MTF design in tangential direction, in sagittal and the average value of every characteristic points are given, respectively.

The grid distortion of the optical system is shown in Fig. 4. The grid images of the paraxial ray and the actual ray almost coincides, and the maximum distortion of the system is 2‰, the relative field is relative to (equivalent) object height is given in Table 3.

3.1.2 Mirror Testing Scheme

The testing scheme of the aspheric mirror is an important part of optical system design. The rationality of the testing scheme determines the achievability of the optical system.

The PM and TM are the off-axis concave mirrors, and the SM is the off-axis convex mirror. The Offner compensators are implemented in the PM and TM surface error testing scheme. The PM testing compensator is designed with two pieces of lens, and the TM testing compensator is designed with three pieces of lens; all the lenses are manufactured with fused silica. The optical design of PM and TM testing are shown in Fig. 5, and the PM and TM testing experiments are shown in Fig. 6.

To avoid manufacturing a bulky large-size Hindle spherical mirror, the SM aspheric surface shape error testing is operated from the back of the SM, which is processed into a flat

Table 3 Relative field is relative to (equivalent) object height (unit:mm)

Normalized field of view in sagittal direction	Normalized field of view in tangential direction	Paraxial image height in sagittal direction	Paraxial image height in tangential direction	Real image height in sagittal direction	Real image height in tangential direction	Sagittal Distortion (%)	Tangential Distortion (%)
−1	1	80.995	−48.029	80.872	−47.940	−0.16	−0.01
−0.5	1	40.498	−48.029	40.466	−47.984	−0.09	−0.01
0	1	0.000	−48.029	0.000	−47.999	−0.06	0
0.5	1	−40.498	−48.029	−40.466	−47.984	−0.09	0.01
1	1	−80.995	−48.029	−80.872	−47.940	−0.16	0.01
−1	0.5	80.995	−24.014	80.897	−23.969	−0.13	−0.02
−0.5	0.5	40.498	−24.014	40.480	−23.999	−0.05	−0.01
0	0.5	0.000	−24.014	0.000	−24.009	−0.02	0
0.5	0.5	−40.498	−24.014	−40.480	−23.999	−0.05	0.01
1	0.5	−80.995	−24.014	−80.897	−23.969	−0.13	0.02
−1	0	80.995	0.000	80.908	0.019	−0.11	−0.02
−0.5	0	40.498	0.000	40.487	0.005	−0.03	−0.01
0	0	0.000	0.000	0.000	0.000	0	0
0.5	0	−40.498	0.000	−40.487	0.005	−0.03	0.01
1	0	−80.995	0.000	−80.908	0.019	−0.11	0.02
−1	−0.5	80.995	24.014	80.901	24.012	−0.11	−0.03
−0.5	−0.5	40.498	24.014	40.485	24.016	−0.02	−0.02
0	−0.5	0.000	24.014	0.000	24.017	0.01	0
0.5	−0.5	−40.498	24.014	−40.485	24.016	−0.02	0.02
1	−0.5	−80.995	24.014	−80.901	24.012	−0.11	0.03
−1	−1	80.995	48.029	80.875	47.996	−0.13	−0.03
−0.5	−1	40.498	48.029	40.474	48.020	−0.04	−0.02
0	−1	0.000	48.029	0.000	48.027	0	0
0.5	−1	−40.498	48.029	−40.474	48.020	−0.04	0.02
1	−1	−80.995	48.029	−80.875	47.996	−0.13	0.03

craft surface. With the Offner compensator composed of two small lenses, the testing operation becomes convenient. The testing optical path of the SM is shown in Fig. 7, and the SM testing experiment is shown Fig. 8.

The manufacture process of mirrors can be seen in Fig. 9, and the surface errors of PM, SM and TM are 0.0160λ, 0.0165λ and 0.0164λ (λ = 632.8 nm), respectively, as shown in Fig. 10.

3.1.3 Suppression of Stray Light

The suppression of stray light is used here to improve the system's performance, including various means such as:

a) Setting the field stop to suppress the stray light out of the imaging FOV;
b) Setting the Lyot stop to suppress the stray light outside the aperture as well as the diffracted stray light;

Fig. 6 The PM and TM testing experiments

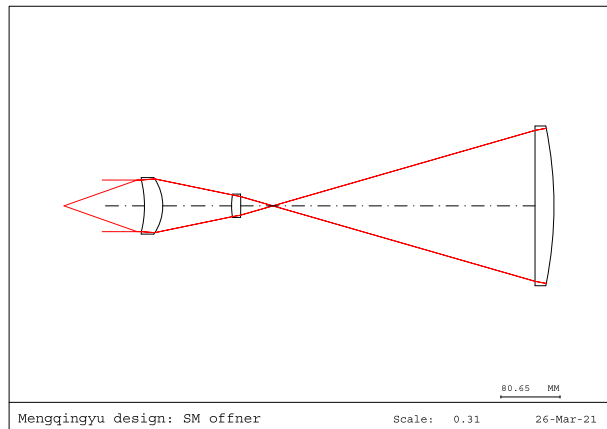**Fig. 7** The optical path design of the SM testing

Fig. 8 The SM testing experiment

c) Minimizing the number of structural parts, to reduce the structural scattered light inside the imaging FOV;
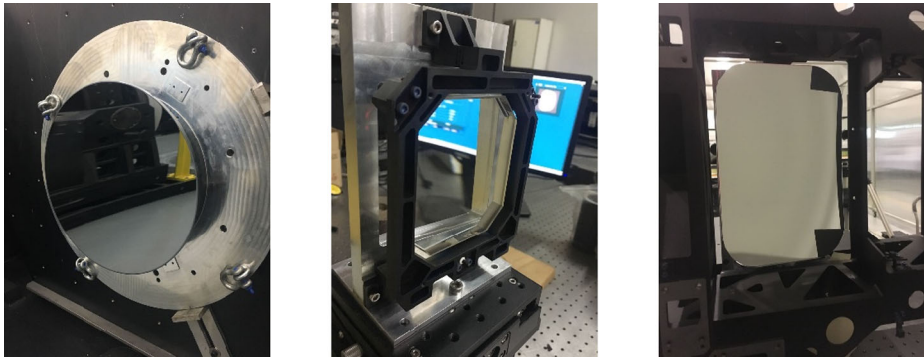
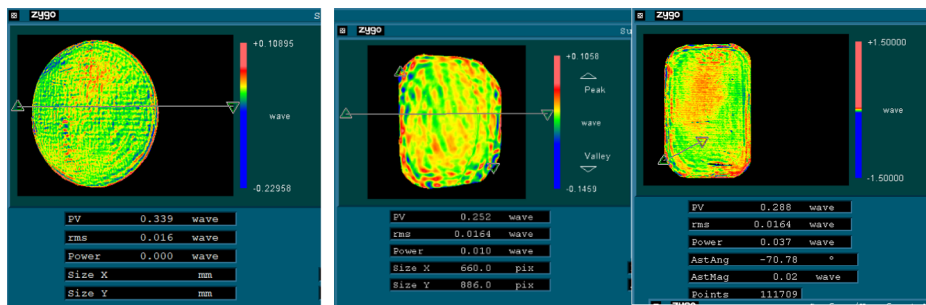**Fig. 9** The manufacture process of PM SM and TM

Fig. 10 PM SM and TM interferometric testing map

d) Reducing the number of optical reflectors and replacing them with low-scattering optical mirrors, to preventing the specular stray light directly entering into the imaging FOV;

e) Setting up the stray light hood and vane.

As shown in Fig. 11, the stray light suppression structure mainly includes three parts: the main hood, the field diaphragm, and the light blocking plates. The structure of suppressing stray light is sprayed by the black extinction coating, whose absorption rate is 95% in the visible spectrum. By the magnetorheological processing technology, the roughness of the mirrors are less than 3 nm, and the mirror surfaces cleanliness are CL800. By using stray light analysis software, the ray in all directions outside the FOV was traced and the stray light paths were analyzed, as shown in Fig. 12. The Point source transmittance curve is shown in Fig. 13. Interpolation and integration calculation of the PST curve shows that its stray light coefficient is 1.71%. Taking into account the black extinction coating absorption rate error (2%), the system's stray light coefficient is 2.39%.

3.2 Opto-Mechanical Structure

The opto-mechanical structure of HiRIC can provide support for its optical, electronics and thermal control systems, and is the basis for realizing various functions of HiRIC. It must not only meet the requirements of the system's general performance indicators, but also satisfies the space environment needs, such as lightweight, compact size, stability and easy adjustment (Ebben et al. 2007).

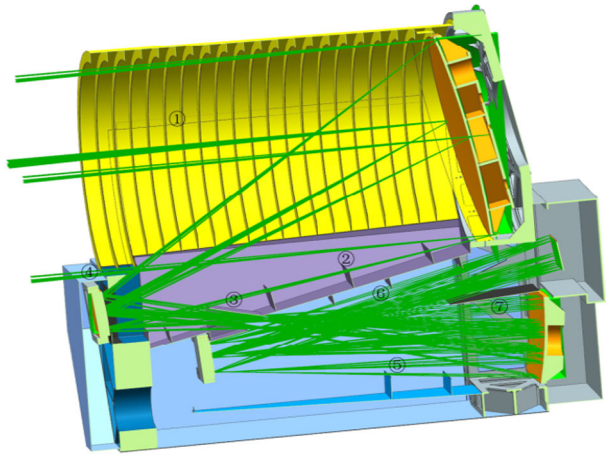**Fig. 11** Stray light suppression
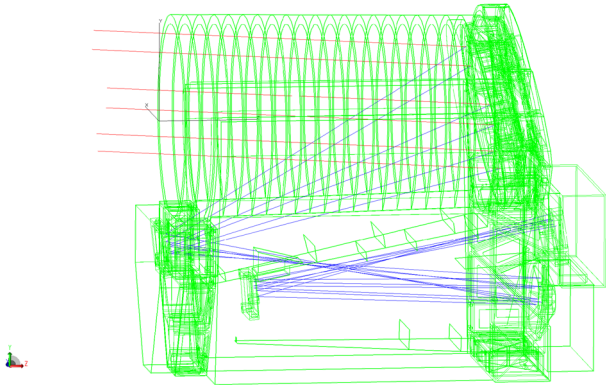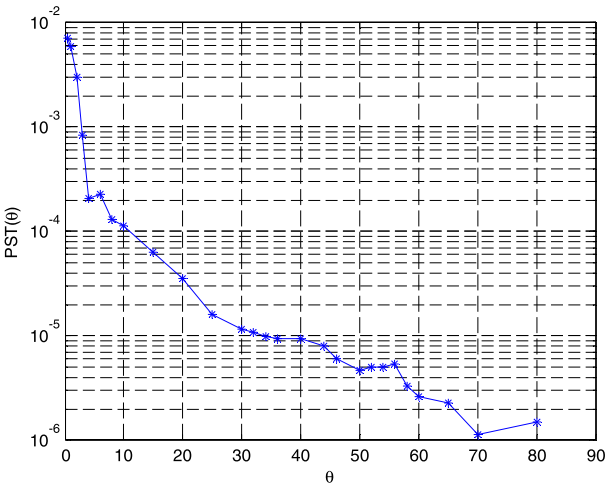mechanical structure

Fig. 12 Stray light path

Fig. 13 PST curve

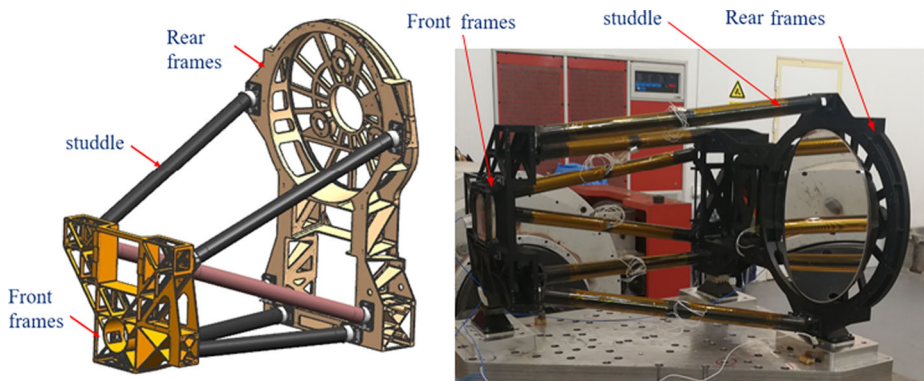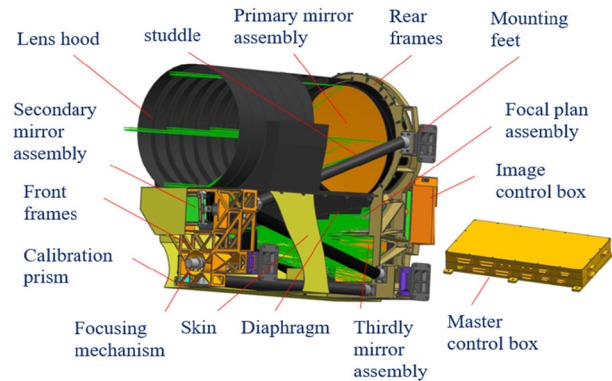**Fig. 14** Optical-mechanical composition of HiRIC

Fig. 15 Bracing Truss Structure

3.2.1 Support Scheme and Detailed Structural Design

The main structure of the HiRIC is composed of the camera and the master control box, as shown in Fig. 14. The camera mainly includes truss structure (front and rear frames and carbon fiber studdle), optical components (primary mirror, secondary mirror, thirdly mirror, focusing mirror), focusing mechanism, focal plan assembly, imaging control box, lens hood, skin, diaphragm and mounting feet.

Considering the requirements of high rigidity and lightweight, the opto-mechanical structure uses a truss structure composed of a front frame, a rear frame and studdles, as shown in Fig. 15.

The front and rear frames are made of high-volume fraction SiC-Al composite materials (60SiC/Al), which adopt a lightweight structure composed of high-strength stiffeners and thin walls, with high specific stiffness. The front and rear frames can provide mounting interfaces and datum to the optical, electronic, and thermal control components, and connect the HiRIC to satellite platforms. The studdles are hollow tubular structures made of carbon fiber composites material (M40J) with high specific stiffness. Two adjacent studdles form a stable triangle by connecting the studdles' pedestal with the front and rear frames. By optimizing the inner and outer diameters as well as the connection angles of the studdles, we can not only improve the structural stiffness and resonance frequency of the frames components, but also guarantee the accuracy of the optical components' positions. In order

Fig. 16 Schematic diagram of focusing mechanism
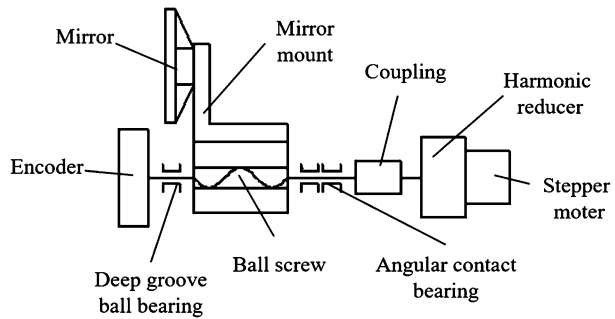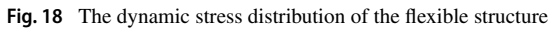

Fig. 17 The finite element model of HiRIC
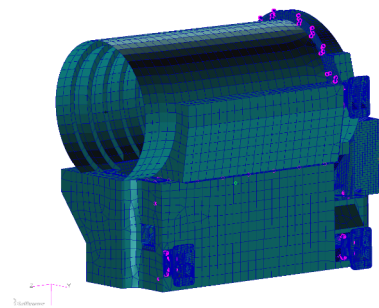
to ensure the geometric position relationship, the shape and the position tolerance between the front and rear frames, three adjustment pads have been added to the connection position. The thickness and inclination of the pads can be adjusted to improve the relative position accuracy and parallelism tolerance of the reference planes.

3.2.2 The Focussing Mechanism Design

The focusing mechanism was mainly composed of a driving component, a motion execution component, a measuring component and a supporting frame, as shown in Fig. 16. The driving component was driven by a stepping motor, and the motor was equipped with a harmonic reducer. The motion execution assembly chose the mode of ball screw drive and linear bearing guide. The measurement module chose the 18-bit absolute encoder produced by Israeli Netzer company. The supporting frame is made of titanium alloy, which has good strength and stiffness, light weight and good dimensional stability. The encoder rotating 360° corresponds to a focusing stroke of 4 mm, and the total focusing error of the focusing mechanism is 4.7 μm.

3.2.3 Simulation Analysis

In the engineering fields, the finite element simulation is now becoming more and more widely used to find design defects and conduct the performance evaluation of design schemes (Gao and Zhang 2018). Therefore, we have established the finite element model of the HiRIC's opto-mechanical structure (as seen in Fig. 17). The static and dynamic simulation of the design is carried out on the finite element modal. The static simulation includes the influence analysis of imaging quality on the gravity load and temperature load, the influence analysis of imaging quality with the structure distortion of the flange face on which

Fig. 18 The dynamic stress distribution of the flexible structure

the camera installed in orbit,the influence analysis of imaging quality with the temperature difference of the flange face on which the camera installed and camera in orbit. The dynamic simulation includes modal analysis, the acceleration analysis, sinusoidal vibration analysis and random vibration analysis.

The influence analysis of imaging quality on the gravity load of 1 g and temperature load of 2°C shows that the MTF of optical system goes down by 2.36% which is smaller than the index of 5%.

The influence analysis of imaging quality with the structure distortion about 0.01 mm of the flange face on which the camera installed in orbit shows that the MTF of optical system goes down by 3% which is smaller than the index of 5%.

The influence analysis of imaging quality with the temperature difference which is generated because the temperature of the flange face on which the camera installed is 0°C and the temperature of the camera is 20°C in orbit shows that the MTF of optical system goes down by 3.5% which is smaller than the index of 5%.

The deformation of the opto-mechanical structure with the above load will lead to the reduction of the MTF of optical system which is smaller the index.

The modal analysis shows that the camera has a reasonable distribution of modal, the fundamental frequency is 73 Hz, which is higher than the requirement of 70 Hz.

The acceleration analysis, sinusoidal vibration analysis and random vibration analysis shows that the maximum dynamic stress which appears in the groove of the flexible structure is 519 MPa which is smaller than the allowable stress of 690 MPa, the dynamic stress distribution of the flexible structure is shown in Fig. 18. The local position with red of flexible structure is the position with maximum stress.

At the same time, the mechanical environment tests, including the acceleration test, sinusoidal vibration test and random vibration test, were carried out on the main opto-mechanical structures. The experiment results are basically consistent with the simulation analysis. The Fig. 19 shows the environment of mechanical test.
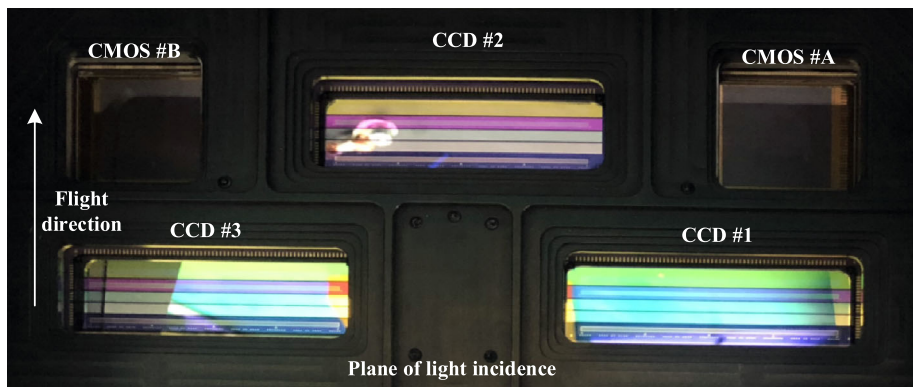
Fig. 19 Mechanical environment test

Fig. 20 Diagram of the detectors on the focal plane

3.2.4 Conclusions

HiRIC was connected to the satellite platform of orbiters via mountings fixed on the side of the HiRIC with freedom release function to avoid deformation of the camera optical components caused by factors such as the static connection between the camera and the surround platform and reduced inconsistent temperature deformation.

The main control box, manufactured with high-specific-stiffness Mg-Al alloy, is separately installed on the platform, and it also adopts a laminated structure with multiple plates and frame seam allowance overlapping.

To be more specific, the opto-mechanical structures are manufactured with SiC, due to the weight and thermal stability concern. And the mechanical structure materials are mainly composed of carbon fiber composite materials and SiC-Al composite materials. In other words, all the mechanical structures are fully carbonized, which guarantees their good thermal matching, great thermal stability and high specific stiffness, and can achieve deep space exploration with an ultra-light weight load. The total weight of the whole main opto-mechanical structures and the master control box is as low as 42 kg.

Table 4 The main specifications of the TDI CCD Detector

No.	Parameter	Parameter value
1	Pixel size	Panchromatic band: 8.75 μm × 8.75 μm
		B band (B1 B2 B3 B4): 35 μm × 35 μm
2	Active Pixels	Panchromatic band: 6144
		B band (B1 B2 B3 B4): 3072
3	Spectral response	Panchromatic band (P): 450 nm∼900 nm
		Blue band (B1): 450 nm∼520 nm
		Green band (B2): 520 nm∼600 nm
		Red band (B3): 630 nm∼690 nm
		NIR band (B4): 760 nm∼900 nm
4	Max line rate	Panchromatic band: 15.85 kHz/30.90 kHz[a]
		B band (B1 B2 B3 B4): 8.00 kHz/15.73 kHz[a]
5	Selectable number of stages	Panchromatic band (P): 8,16,32,48,64,96
		Blue band (B1): 4,16,32,48,64
		Green band (B2): 4,12,24,32,48
		Red band (B3): 4,8,16,24,32
		NIR band (B4): 4,8,16,24,32
6	Dynamic range	54 dB
7	Number of taps	4/8[a]
8	Max data rate per tap	25 MHz

[a]Indicates parameter values in bidirectional readout mode.

3.3 Detectors

The imaging focal plane of the HiRIC is composed of three linear array TDI CCD detectors and two area array CMOS detectors as shown in Fig. 20. As we mentioned above, the orbiter carries the HiRIC around the Mars in an elliptical orbit. When it moves to perigee, the TDI CCD detectors start to work and acquire the high-resolution local imaging details of the Martian surface. In addition, the CMOS detector can image the Mars with video format.

To increase the imaging widths, the three TDI CCD detectors are installed with staggered splicing, which is a mature solution in aerospace remote sensing systems (Irons et al. 2012).

3.3.1 The TDI CCDs

The primary task of the HiRIC is to obtain the detail images of Martian surface, which means the imaging should be highly sensitive and have high signal-to-noise ration. For this purpose, the multispectral TDI CCDs customized by Teledyne DALSA company are used, which can work in five independent spectral bands of panchromatic, blue, green, red and near infrared. The main specifications are shown in Table 4.

With proper optical design, the detector can acquire 0.5-m resolution images of the Martian surface under panchromatic mode. Under the multi-spectral modes, the equivalent 2 × 2 binning mode (1 × 2 charge domain binning along the scanning direction, and 2 × 1 digital domain binning in the orthogonal direction) functions to achieve 2-m resolution images. The panchromatic image data are set as 3 times more than multi-spectral image data, to facilitate image fusion. The pixel number under the panchromatic mode is 6144, and each two adjacent detectors are mechanically spliced with an overlap of 116 pixels. Therefore,

Table 5 The main specifications of the HR400 CMOS Detector

No.	Parameter	Parameter value
1	Pixel size	11 μm × 11 μm
2	Active Pixels	2048 × 2048
3	Shutter type	Electronic rolling shutter
3	Spectral response	400∼1000 nm
4	Frame rate	48 fps@STD mode
		24 fps@HDR mode
5	Dynamic range	96 dB (HDR mode)
6	Effective number of bits (ENOB) of ADC	12-bit

the equivalent pixel number of the spliced TDI CCD detectors is 18200, corresponding to a 9 km push-broom imaging width.

When reading out the pixels horizontally, the detector has unidirectional and bidirectional modes, corresponding to 4-tap and 8-tap output in the panchromatic band, respectively. At the orbital altitude of 265 km (the required testing altitude of the Tianwen-1), the image motion matching frequencies of the panchromatic band and the multi-spectral bands are 8.1 kHz and 2 kHz, respectively. Therefore, the unidirectional mode is less complex and sufficient to meet the readout needs. It must also be mentioned that the readout noise directly increases with the pixel readout rate, hence in our design, the readout rate is lowered as possible. The readout rates are set as 14 MHz and 7 MHz for the panchromatic band and the multi-spectral bands, respectively.

To improve its reliability, the HiRIC is designed to have three separate electrical channels, each contains power circuits, driving circuits, data acquisition and transmission circuits. CCD #1 and CMOS #A share the same back-end circuit, CCD #3 shares the circuit with CMOS #B, and CCD #2 uses a circuit independently.

3.3.2 The CMOS

As a supplement to the HiRIC's operation mode, the CMOS detector is implemented to undertake frame imaging. The HR400 CMOS detector by Gpixel Inc. is used, and its main specifications are shown in Table 5.

The detector has two imaging modes: Standard (STD) and High Dynamic Range (HDR). In our design, the HDR mode is adopted, in which the frame rate can reach up to 24 fps.

3.4 Thermal Control

3.4.1 Orbit Thermal Environment Analysis

The main goal of thermal design is to ensure the temperature requirements of the camera during its lifetime. After launching, the HiRIC will go through the Earth-Mars transition stage, the Mars capturing stage, and the Mars orbital stage. During the whole flight, the satellite is oriented towards to the sun with the +X axis, while the camera has no external heat flow. The camera runs in an elliptical orbit, whose perigee height is about 265 km, and orbital period is about 7.8 hours. The camera will obtain images when orbital altitude is below 800 km and conditions are suitable. During camera operation, the optical axis (+Z axis) is oriented to Mars, and −Z axis is oriented to the sun during other periods. During

the camera's optical axis oriented to Mars, the camera has a little solar albedo energy and Mars infrared radiation energy. The camera has no external heat flow during -Z axis oriented to the sun. Therefore, the camera has a low external heat flow input throughout its lifetime. The camera's thermal control design is mainly based on thermal insulation design, while ensuring temperature uniformity and stability requirements.

In order to prevent the camera's optical axis from being oriented to the sun, which can cause damage to the camera, a solar exclusion angle (minimum angular distance between camera pointing direction and sun) was defined. Through thermal simulation analysis, the solar exclusion angle was set as 30°.

3.4.2 Temperature Index and Thermal Design Constraints

According to the requirements of Tianwen-1, the working temperature of the camera should be 18 ± 2 °C when imaging and its axial temperature difference should be less than 2 °C. During the imaging storage, the temperature of the camera body should be -5 °C$\sim +45$ °C. The working temperature of the camera's mounting interface should be 0 °C-30 °C and -30 °C-20 °C during imaging time and the storage time, respectively.

Also, the power consumption for thermal control could not exceed 60 W during working hours, taking the consumption of the control box into account. The power consumption of the compensation thermal design could not exceed 38 W during non-working time. Due to the limited energy, the thermal control system will be powered off for 2 hours during Mars's shadow area which will occur during non-working time, and the equipment temperature should meet the requirements of storage temperature during the power outage.

3.4.3 Imaging Electronics Thermal Design

The total heat consumption of the imaging electronics is about 105 W during working time, but the working time does not exceed 2 min in an orbital period. Therefore, the heat energy will be consumed locally. In our design, the heat dissipation path is: CCD → backplane → focal plane substrate → rear frame. Through the designed path, the heat generated by the electronic elements is directly transmitted to the rear frame.

3.4.4 Thermal Design of the Camera Body

The thermal design of the camera body combines active and passive thermal control measures. The passive thermal design mainly includes thermal isolation off the space environment, the satellite platform, the low-temperature hood and the low-temperature diaphragm. The active thermal control includes the temperature closed-loop control and compensation thermal design. The active thermal control mainly works before imaging to ensure the temperature demand to image. Meanwhile, the compensation thermal design, which is directly powered by the Orbiter platform, is adopted to reduce the thermal control power consumption during the non-working period (Iwata et al. 2012).

Thermal Insulation Design of the Camera Body As shown in Fig. 21, the camera body is insulated from the Orbiter platform through three low-thermal-conductivity carbon fiber brackets. The surface of the camera is covered by MLI and thermal insulation pads to reduce the influence from external thermal environment. Six carbon fiber rods and the front frame are coated with MLI to avoid heat leakage to low-temperature hood.

Fig. 21 Thermal design diagram of the hood
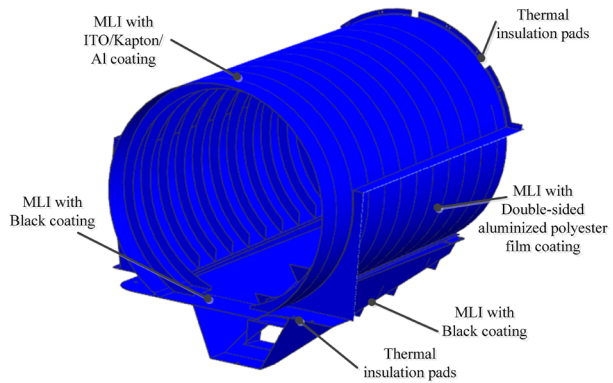
Table 6 Distribution of active heat circuits design

No.	Heating zone	Sensor location	Temperature target (°C)	Power (W)
1	Skin of front frame	Middle of front frame	18.0	12
2	skin of secondary mirror	Back of secondary mirror	18.0	2
3	skin of focusing mirror assembly	back of focusing mirror	18.0	2.5
4	Carbon fiber rod 1	Middle of carbon fiber rod 1	18.0	1
5	Carbon fiber rod 2	Middle of carbon fiber rod 2	18.0	1
6	Carbon fiber rod 3&4	Middle of carbon fiber rod 3	18.0	1
7	Carbon fiber rod 5&6	Middle of carbon fiber rod 5	18.0	1
8	Skin of camera +Y direction	Skin of camera +Y direction	17.0	4.5
9	Skin of camera −Y direction	Skin of camera −Y direction	17.0	4.5
10	Heating cover of primary mirror −X direction	Cover of primary mirror −X direction	18.5	3
11	Heating cover of primary mirror +X direction	Cover of primary mirror +X direction	18.5	4
12	Middle of rear frame	Middle of rear frame	18.0	4.5
13	Skin of rear frame +Y direction	Rear frame +Y direction	18.0	4
14	Skin of rear frame −Y direction	Rear frame −Y direction	18.0	2
15	Skin of third mirror	Rear frame +X direction	17.5	4
16	Skin of rear frame −X direction	Rear frame −X direction	18.5	9

Active Thermal Design The camera has a total of 16 active heat circuits, whose distribution can be found in Table 6.

Compensated Heating Design Compensated heating is powered by the satellite platform. The heating areas are allocated in front frame (13 W), carbon fiber rods (3 W), rear frame −X direction (14 W), and rear frame +X direction (8 W). The temperature switches are series connected in the heating circuits, whose locations are shown in Fig. 22. In order to meet the temperature requirement during outage period for 2 hours, the operating temperature range of the temperature switch is selected closed below 5 °C and opened above 16 °C.
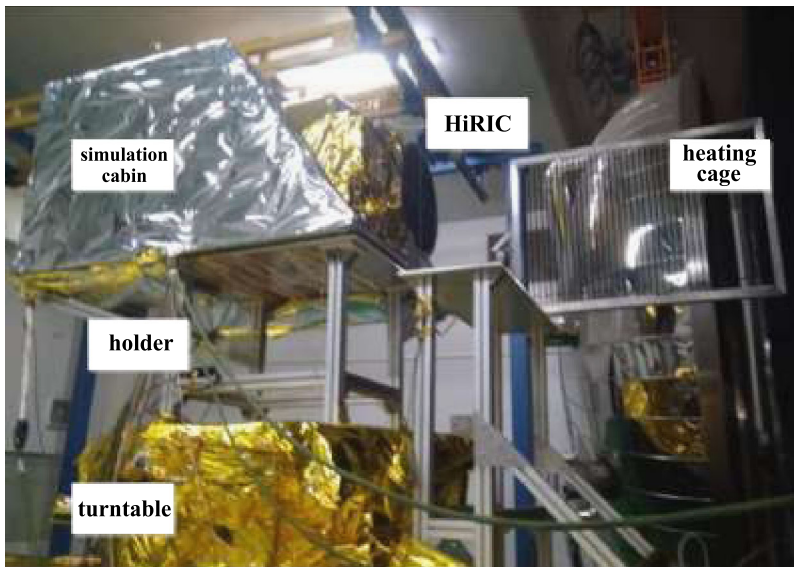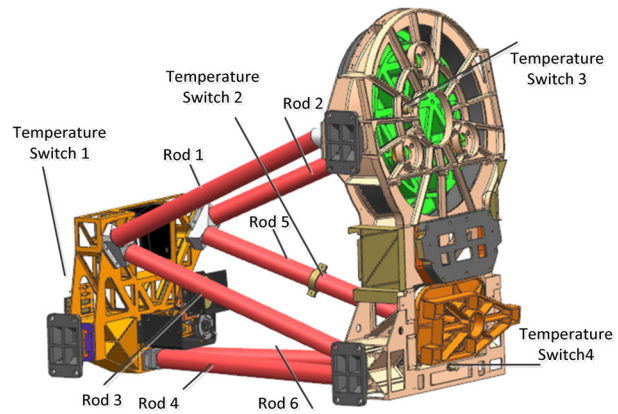
Fig. 22 Layout of temperature switches

Fig. 23 High-resolution camera before entering the vacuum tank

3.4.5 Thermal Balance Test Results

In order to verify the reliability of the thermal design, a thermal balance test was carried out, as shown in Fig. 23. We built up a simulation cabin and an infrared heating cage to simulate the thermal environment of the HiRIC. Extreme temperature conditions, including low-temperature storage condition, low-temperature working conditions and high-temperature working condition (as shown in Table 7), have been considered.

Testing results (as shown in Table 8) showed that thermal control system could meet the requirement of Tianwen-1. The camera's temperature is higher than 10 °C in the low-temperature storage mode. Optical temperature fluctuations were at $18 \pm 1°C$ and axis temperature difference meets the requirements during working conditions. The total thermal control power consumption was no more than 52.2 W, which met the requirements of Tianwen-1.

Table 7 The extreme conditions in the heat balance test

Working conditions	Interface temperature (° C)	Solar heat flux (W/m^2)	Mars infrared heat flux density in working arc (W/m^2)	Solar albedo in working arc	Altitude definition	Thermal control mode	Imaging mode
Low-temperature storage	−35	NA	NA	NA	−Z orientation to the sun	Compensated heating	Not working
Low-temperature working	−5	493	30	0.25	Near Mars +Z to Mars, Far Mars −Z to the sun	Active heating	Working near Mars
High-temperature working	35	717	354	0.29	Near Mars +Z to Mars, Far Mars −Z to the sun	Active heating	Working near Mars

Table 8 Results of the heat balance test

Component		Low-temperature storage conditions	Low-temperature working condition	High-temperature working condition
Temperature fluctuation (°C)	Primary mirror	15.0	17.5∼17.6	17.1∼17.5
	Secondary mirror	15.8	18.0∼18.1	18.0∼18.1
	Third mirror	16.2	18.1∼18.2	18.5∼18.6
	Main frame	10.1∼17.5	17.5∼18.5	17.5∼18.5
Thermal control power (W)		38	52.2	37.7

3.5 Data Processing Unit (DPU)

The DPU consists of an Imaging Module and a Control Module, as shown in Fig. 24. The Imaging Module is installed at the rear of the focal plane components of the camera body, and it is close to the focal surface components, which mainly complete imaging and storage functions of the camera's CCD and CMOS. The Control Module is installed on the satellite platform, as close as possible to the camera body. It is connected to the HiRIC body by cables.

The Imaging Module consists of three CCD Boards, three CMOS Boards, three Processor Boards, a CCD Driver Board, two CMOS Driver Boards, a Control Board, and a Storage Board. The Control Board is mainly composed of FPGA and other interface circuits. These interface circuits are used to generate clock signals for CCD and CMOS operation, receive data from CCD and CMOS, communicate with peripheral circuits. The Storage Board puts the CCD and CMOS image data into 6 Nand-flash through a High Speed Low-Voltage Differential Signaling (LVDS) connector from the Control Board. When the data is demanded, it will transmit to the Payload Controller by LVDS.

The Control Module includes a Control Board, a Secondary Power Board, a Thermal Control Board, a Focal Plane Interface Board. Inside of them, the Control Board, the Secondary Power Board and the Thermal Control Board are designed by using cold backup to improve the reliability of the system. The Control Board adopts an anti-irradiation architecture (DSP + FPGA, the FPGA uses an anti-fuse structure), receives the Payload Controller
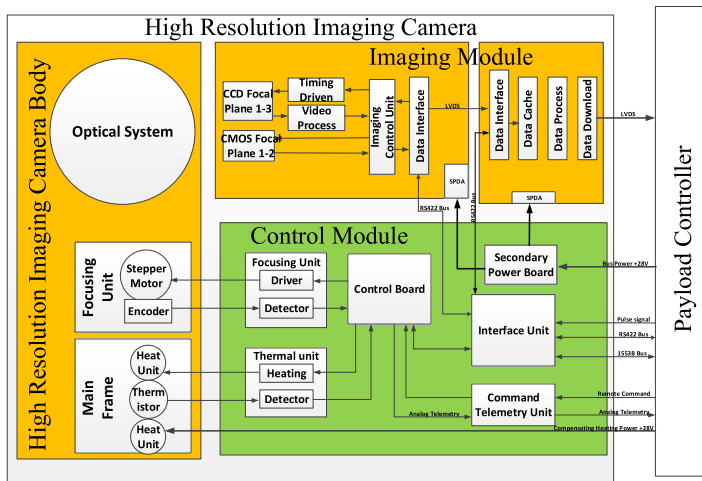
Fig. 24 The systematic diagram of HiRIC

data through the 1553B bus, and transmits relevant command to the Focal Plane Interface Board through the 422 bus. The Secondary Power Board supply various voltages to each system by power conversion module,such as the fuse protection circuit, the soft-start circuit and the DC/DC conversion circuit; The Thermal Control Board gets the temperature information by the method which mainly uses a voltage supplied by precision power, an accurate AD sampling temperature acquisition circuit and a gate circuit unit. A stepper motor and an absolute encoder are controlled by Focal Plane Interface Board through the subdivision algorithm, which achieve smooth control of the motor (Donald et al. 2005).

4 Testing, Calibration, and Performance

4.1 Calibration

Before the calibration of HiRIC, a total of 62 items were required to be tested first, including optical imaging quality, optical-mechanical structure performance, detecting component performance and so on.

The above-mentioned testing contents are combined with various environmental tests in the process of development. The stability of camera function and performance under various environmental conditions is reflected by comparing the testing results.

After completing all the testing work, the calibration of HiRIC was carried out, including geometric calibration, radiometric calibration, spectral calibration and color calibration.

The purpose of geometric calibration is mainly to obtain the information of the camera's principal point, principal distance, distortion and coordinate transformation relation. The calibration precision of the principal point is better than 0.002 mm, the calibration precision of the principal distance is better than 0.05%, and the calibration precision of the relative distortion is better than 0.3%.

The aim of radiometric calibration is to calibrate and optimize the non-uniformity and non-linearity of radiation response of detector, in which the relative radiometric calibration
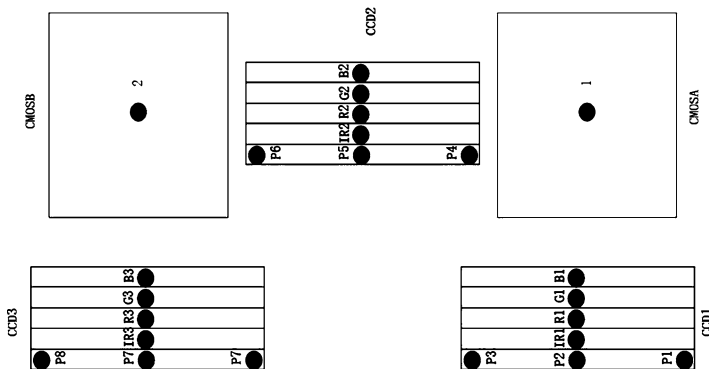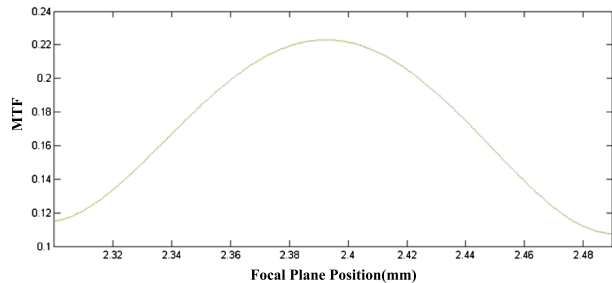
Fig. 25 Schematic diagram of different testing FOV points


Fig. 26 Focusing curve of CCD1

uncertainty is better than 3% and the absolute radiometric calibration uncertainty is better than 7%.

The purpose of spectral calibration is to determine the spectral response function of a high-resolution camera to monochromatic light, the central wavelength and spectral resolution of each sampling channel for spectral detection, etc., the spectral range of the HiRIC includes 5 spectral ranges: panchromatic 0.45 μm ∼ 0.9 μm, blue 0.45 μm ∼ 0.52 μm, green 0.52 μm ∼ 0.60 μm, red 0.63 μm ∼ 0.69 μm and near-infrared 0.76 μm ∼ 0.90 μm, the calibration accuracy (central wavelengths) is better than 30 nm@panchromatic, 15 nm@blue, 15 nm@green, 15 nm@red and 20 nm@near infrared. The main purpose of color calibration is to obtain the color correction coefficient so that the color correction effect of the images acquired by the camera is consistent with the visual perception of human eyes.

4.2 Modulation Transfer Function (MTF)

In order to accurately reflect the imaging quality of HiRIC in orbit, a thermal-optical experiment was designed to test the MTF of the HiRIC at 11 °C, 16 °C, 18 °C, 20 °C and 25 °C respectively, the camera's technical status before its testing in the vacuum tank is shown in Fig. 23. The FOV points for HiRIC MTF testing are shown in Fig. 25.

The relationship between the MTF of HiRIC and the focal plane position in equilibrium (18 °C) is shown in Figs. 26, 27 and 28.

Fig. 27 Focusing curve of CCD2
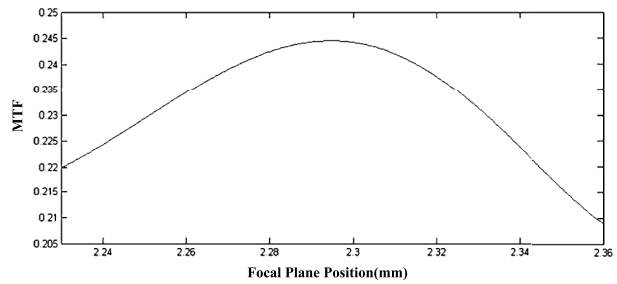
Fig. 28 Focusing curve CCD3
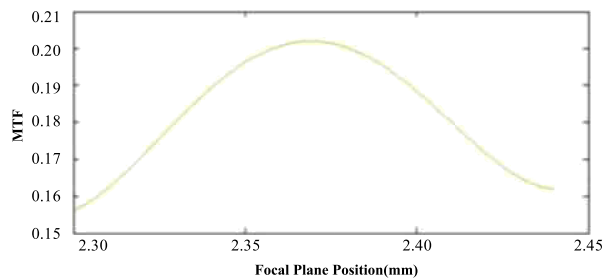
Fig. 29 The stimulated calibration site
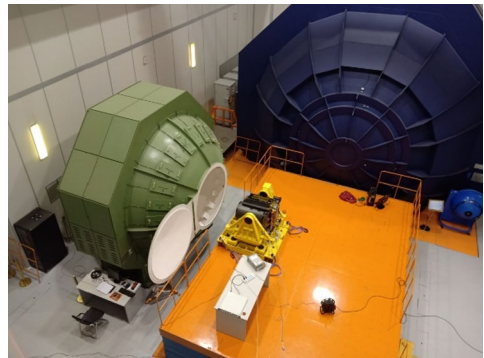
4.3 Signal-to-Noise Ratio

According to the Tianwen-1's requirements, the signal-to-noise ratio (SNR) of the HiRIC should be no less than 100 under the extreme illumination conditions of 265 km orbit altitude, where the solar elevation angle is 30 degrees and the ground Albedo is 0.2. Therefore, as shown in Fig. 29, we simulated the extreme illumination conditions brightness of the camera by integrating sphere calibration light source in the laboratory, and then tested its signal-to-noise ratio.

Under the extreme illumination conditions of 265 km orbit altitude, the solar elevation angle is 30 degrees and the ground Albedo is 0.2, the average signal-to-noise ratio (SNR) of the full spectrum is 109.97 (if the integral stage of TDICCD is 32) or 143.97 (if the integral stage of TDICCD is 48).

Table 9 Working modes of HiRIC

No.	Modes	Definition	Working conditions
1	Imaging	Including Panchromatic (Default), Colors, Full spectrum, CMOS and customize mode	The orbit altitude is below 800 km and the solar elevation angle is greater than 10°; Flies over the landing sites or areas of interest
2	Health Check	Including master control check, imaging check and storage/processing check	Once one or two months
3	Thermal control	Including compensation heating, typical heating, and data injected heating	Compensation heating used in transfer orbit; Typical heating used to ensure the normal work of the camera; Injected heating used to test camera performance
4	Focusing	Including focusing and non-focusing	Using as needed

5 Working Modes and Inflight Scientific Exploration Programs

5.1 Working Modes

There are 4 working modes for HiRIC as listed in Table 9, in which imaging is its main scientific exploration mode inflight.

The specific contents of the imaging mode are shown in Table 10.

HiRIC plans to use panchromatic band as the default imaging mode to obtain high-resolution images of the landing site and areas of interest on the Martian surface (McEwen et al. 2017b; Carr 2007; Barlow 2014; McEwen et al. 2017a, 2007; Dundas et al. 2010; Bondarenko et al. 2014). With the input parameters from the ground, CCDs can obtain push-broom image data directly, and store them in the internal storage units of HiRIC in real time. The images will be downlinked to the ground when available. Input parameters mentioned here including the functioning CCD, imaging spectrum, integration series, gain and line frequency. For CMOS imaging mode, the two CMOSs can work at the same time, and parameters including integration time and frame rate also can be customized.

According to the design orbit, the ground velocity of Tianwen-1 orbiter will vary from 4.02 to 3.07 km/s when the orbit altitude is below 800 km, among which the velocity can reaches a maximum value of 4.02 km/s at the perigee and the data rate of HiRIC will reach the maximum at this moment. The corresponding pixel resolution will be 0.5 m and 2 m for panchromatic and colors imaging mode respectively with an image swath width of 9 km. A total of about 8040 and 2010 line of images can be obtained for the two imaging mode per second. Based on 6144×3 pixels per line (panchromatic mode) and 1536×3 pixels (colors mode), 12 bits per pixel quantized calculation, the data rate of each spectral band images is as shown in Table 11. Table 11 also showed the data rate for HiRIC images under a 4*4 binning imaging condition, corresponding to panchromatic band images with a resolution of 2.0 m and color band images with a resolution of 8.0 m.

It can be seen from the above table that the maximum amount of data of HiRIC will be generated when it reaches the perigee. At present, HiRIC is planned to obtain push-broom image data for about 120 km each time, and the continuous imaging time will be 30 s near the perigee. So the amount of data generated in the default imaging mode will be

Table 10 Imaging mode of HiRIC

No.	Modes	Definition	Working conditions
1	Panchromatic (Default)	Pixel resolution: 0.5 m@265 km Swath width: 9.0 km@265 km	1) 3 CCD images; 2) Non-binning; 3) Image resolution: 0.5 m@265 km; 4) Image Swath width: 9 km@265 km; 5) ENOB: 12 bits
2	Colors (BL/RE/GR)	Pixel resolution: 2.0 m@265 km Swath width: 9.0 km@265 km	1) 3 CCD images; 2) Non-binning; 3) Image resolution: 2.0 m@265 km; 4) Image Swath width: 9 km@265 km; 5) ENOB: 12 bits
3	Full spectrum (Panchromatic BL/RE/GR/IR)	Pixel resolution: Panchromatic 0.5 m/@265 km BL/RE/GR/IR 2.0 m@265 km Swath width: 9.0 km@265 km	1) 3 CCD images; 2) Non-binning; 3) Image resolution: Panchromatic: 0.5 m@265 km; BL/RE/GR/IR: 2.0 m@265 km 4) Image Swath width: 9 km@265 km; 5) ENOB: 12 bits
4	CMOS	Pixel resolution: 2.5 m@265 km Swath width: 1.2 km × 1.2 km@265 km	1) 4 × 4 binning; 2) Effective pixels: 512 × 512; 3) Image Swath width: 1.2 km × 1.2 km@265 km; 4) ENOB: 12 bits
5	Customize	Can be set	Can be set

Table 11 Data rate for HiRIC images

Mode	Panchromatic 0.45~0.9 nm	BL 0.45~0.52 nm	GR 0.52~0.6 nm	RE 0.63~0.69 nm	IR 0.76~0.9 nm
Data rate under the highest resolution imaging condition, Mbps	1695.938	105.996	105.996	105.996	105.996
Data rate under a 4*4 binning imaging condition, Mbps	105.996	6.625	6.625	6.625	6.625
Data rate under the highest resolution imaging condition after compression (default compression ratio), Mbps	282.656	17.666	17.666	17.666	17.666

1695.938 Mbps × 30 s/6 = 8.281 Gb (1:6 compression). For CMOS mode, the amount of data of each image will be 3 Mb with a frame rate of 25 fps.

HiRIC uses JPEG2000 as its image compression algorithm. For remote sensing images, using the JPEG2000 algorithm can obtain restored images which are more delicate and smooth with richer details and textures than using other algorithms like JPEG, and has a better peak signal-to-noise ratio (PSNR) comparable to image compression algorithms such as SPIHT and CCSDS-IDC. The JPEG2000 algorithm first performs discrete wavelet transformation on the original images, and then performs quantization and entropy coding (EBCOT) on the transform coefficients before forming the output code stream. After the compressed image data stream is stored or transmitted, entropy decoding, inverse quantization and inverse wavelet transform are performed to restore the images. During the on-orbit operation, HiRIC performs data transmission with the probe platform every 512 image lines. Under the compression mode, the images will be compressed in blocks at a minimum resolution of 384 pixels/line so that there will be a total of 16 types of compressed blocks, which recorded as "resolution 1∼16" with the pixel number of (384*N) *512 (N = 1, 2, 3...16). The results of the special compression test and the ground scientific verification test for HiRIC show that its image compression algorithm is correct and feasible, and the compression quality meets the task requirements.

5.2 Inflight Scientific Exploration Programs

### 5.2.1 High-Resolution Imaging of Tianwen-1 Landing Site

The whole mission of Tianwen-1 can be divided into 6 stages, including launch, transferring, Martian capturing, parking, deorbit and landing, and scientific exploration (tracking and data relay orbit/mission orbit). HiRIC will not start its work until parking stage, when it will obtain stereo images of the landing area/landing site to provide its background terrain information for engineering tasks. Since the HiRIC is a linear array push-broom imaging camera, in order to achieve stereo images, the same target needs to be imaged from different angles. The baseline-height ratio of images for terrain reconstruction is recommended to be ≥0.4.

According to the design orbit, the parking orbit of Tianwen-1 mission is a large elliptical orbit with an orbital period of about 2 Martian days. The position of the sub-satellite point remains basically unchanged every time when the orbiter flies over the landing site. So stereo images can be obtained by adjusting the pitch attitude angle of the orbiter before and after it flies over the landing site. At the same time, the coverage of HiRIC images on the landing site can be increased by adjusting the yaw attitude angle of the orbiter.

The spread range of landing site is 40 km (east-west direction) × 100 km (north-south direction). As mentioned above, the image length of the HiRIC will be 120 km with a swath width of 9 km at the perigee so that one image can achieve the coverage of the latitude range of the landing site. However, the coverage of the longitude range needs to be achieved by the pendulum measurement. According to the requirement of longitude overlap coverage of not less than 15%, at least 6 tracks of stereo image data are required to complete the stereo coverage of the landing site. As a result, a total of 12 images are needed for this work (in Fig. 30, two different angle images are obtained in the same area to obtain stereo data). The pixel resolution of the images will be 0.5 m ∼2.0 m near the perigee.

In the tracking and data relay orbit, HiRIC plans to image the actual landing site every three days to ensure that it can image the rover.

Fig. 30 Coverage of HiRIC images on landing site
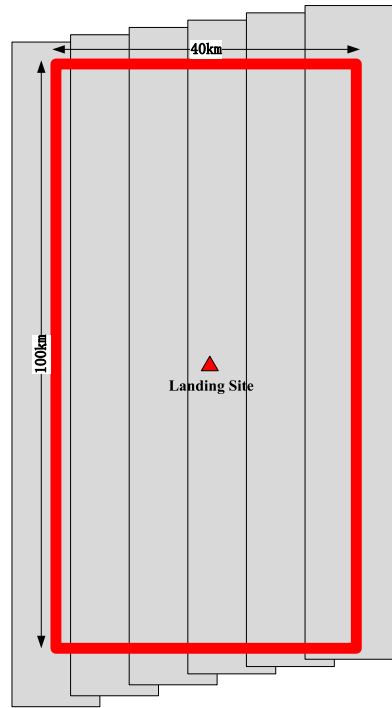
5.2.2 High-Resolution Imaging of Areas of Interests

After the orbiter enters the mission orbit, high-resolution imaging of areas of interest on Martian surface (Bell et al. 2004a,b; Blake et al. 2013) will be the main task of HiRIC. At present, the following selection principle for the areas of interest is initially considered:

1) Typical geomorphic units with characteristic, such as craters, basins, volcanoes, canyons, plains, hilly belts, dry river beds, collapsed landforms, sand dunes, etc.;
2) Geological units with special significance, such as sedimentary rock layer, volcanic structure, rift edge, polar zone sedimentary layer, etc.;
3) Areas that may have dynamic changes, perform multiple high-resolution imaging, and observe the dynamic changes, such as the seasonal changes on the Martian surfaces, the process of glaciers, and the process of sand and dust storms;
4) High-resolution imaging of some typical landforms and geological units that have been released internationally for data feature comparison;
5) The imaging areas of the HiRIC must be co-ordinated with the Mars global imaging task of the medium-resolution camera (MoRIC). Considering the large amount of data, the imaging should be arranged at a time when the distance between the Mars and the Earth is close and the data transmission ability is strong.

Based on the above principles, areas of interest will be selected as HiRIC imaging target. The images can be used as an effective supplement to existing high-resolution images of areas of interest on Martian surface (Grotzinger et al. 2014; Keszthelyi et al. 2008; Lefort et al. 2009), which will further deepen people's comprehensive understanding of Mars.
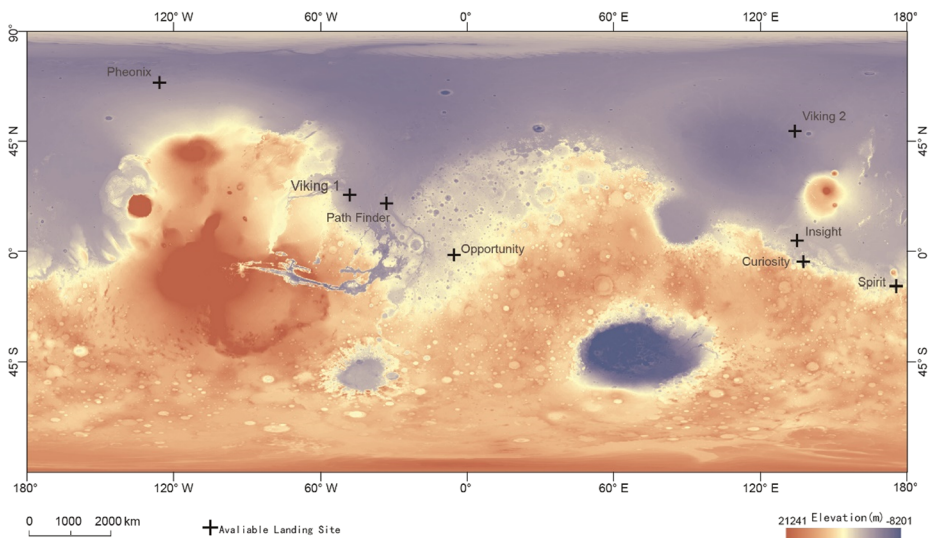
Fig. 31 Landing sites of international Mars missions

5.2.3 High-Resolution Imaging of International Mars Mission Landing Sites

There are currently 8 Mars exploration missions that have successfully landed internationally, as shown in Fig. 31. The HiRIC also plans to image these Martian landing sites (Kirk et al. 2008; Golombek et al. 2012, 2017; Fergason et al. 2017) in the default mode. Each landing site is planned to be imaged once for 10 s with a coverage area of 9 km × 40 km. These images can be used to study dynamic changes on the Martian surface caused by human activity.

6 Conclusions

The HiRIC team has completed the development of the HiRIC on China's First Mars Exploration Mission. The HiRIC applies the COOK off-axis TMA optical system to achieve 0.5 m ground sampling distance at 265 km orbit altitude. To reduce the weight of the HiRIC, the optical-mechanical structure adopts lightweight design, carbon fiber materials are wildly used. The TDI CCD and CMOS detectors are assembled on the image plan to achieve push broom imaging and array imaging. The HiRIC has been designed with precise thermal control to ensure the thermal stability of working in the space environment. By testing, it shows that the HiRIC's various performance indicators are good, and it is ready for launch at time.

This article reports the HiRIC's technical scheme and research results in detail. Tianwen-1 has been successfully launched in July 2020. The HiRIC will obtain high-resolution images of Mars, helping scientists achieve more scientific research results.

References

N. Barlow, *Mars: An Introduction to Its Interior, Surface and Atmosphere* (Cambridge University Press, New York, 2014)

J. Bell III, S. Squyres, R. Arvidson et al., Pancam multispectral imaging results from the Spirit rover at Gusev crater. Science **305**(5685), 800–806 (2004a)

J. Bell III, S. Squyres, R. Arvidson et al., Pancam multispectral imaging results from the Opportunity Rover at Meridiani Planum. Science **306**(5702), 1703–1709 (2004b)

D. Blake, R. Morris, G. Kocurek et al., Curiosity at Gale crater, Mars: characterization and analysis of the Rocknest sand shadow. Science **341**(6153), 1239505 (2013)

N. Bondarenko, I. Dulova, Y. Kornienko, Topography of polygonal structures at the Phoenix landing site on Mars through the relief retrieval from the HiRISE images with the improved photoclinometry method. Sol. Syst. Res. **48**(4), 243–258 (2014)

M.H. Carr, *The Surface of Mars* (Cambridge University Press, New York, 2007)

L. Donald, W. James, A. Martin et al., An overview of the instrument suite for the Deep Impact mission. Space Sci. Rev. **117**, 43–93 (2005)

C. Dundas, A. McEwen, S. Diniega et al., New and recent gully activity on Mars as seen by HiRISE. Geophys. Res. Lett. **37**(7), L07202 (2010)

T. Ebben, J. Bergstrom, P. Spuhler et al., Mission to Mars: the HiRISE camera on-board MRO, in *Proc. SPIE 6690, Focal Plane Arrays for Space Telescopes III*, vol. 66900B (2007)

R. Fergason, R. Kirk, G. Cushing et al., Analysis of local slopes at the InSight landing site on Mars. Space Sci. Rev. **211**(1–4), 109–133 (2017)

Y. Gao, B. Zhang, Design and analysis for the flexible support structure of high precision lens assembly. Optik, Int. J. Light Electron Opt. **175**, 228–236 (2018)

M. Golombek, J. Grant, D. Kipp et al., Selection of the Mars Science Laboratory landing site. Space Sci. Rev. **170**(1–4), 641–737 (2012)

M. Golombek, D. Kipp, N. Warner et al., Selection of the InSight landing site. Space Sci. Rev. **211**(1–4), 5–95 (2017)

J. Grotzinger, D. Sumner, L. Kah et al., A habitable Fluvio-Lacustrine environment at Yellowknife bay, Gale crater, Mars. Science **343**(6169), 1242777 (2014)

J.R. Irons, J.L. Dwyer, J.A. Barsi, The next Landsat satellite: The Landsat Data Continuity Mission. Remote Sens. Environ. **122**, 11–21 (2012)

N. Iwata, T. Usui, A. Miki et al., Thermal control design of X-ray astronomy satellite ASTRO-H, in *42nd International Conference on Environmental Systems* (2012), p. 3579

L. Keszthelyi, W. Jaeger, A. McEwen et al., High Resolution Imaging Science Experiment (HiRISE) images of volcanic terrains from the first 6 months of the Mars Reconnaissance Orbiter primary science phase. J. Geophys. Res., Planets **113**(E4), E04005 (2008)

R. Kirk, E. Howington-Kraus, M. Rosiek et al., Ultrahigh resolution topographic mapping of Mars with MRO HiRISE stereo images: meter-scale slopes of candidate Phoenix landing sites. J. Geophys. Res., Planets **113**(E3), E00A24 (2008)

A. Lefort, P. Russell, N. Thomas et al., Observations of periglacial landforms in Utopia Planitia with the High Resolution Imaging Science Experiment (HiRISE). J. Geophys. Res., Planets **114**(E4), E04005 (2009)

A. McEwen, E. Eliason, J. Bergstrom et al., Mars reconnaissance orbiter's High Resolution Imaging Science Experiment (HiRISE). J. Geophys. Res., Planets **112**(E5), E05S02 (2007)

A. McEwen, C. Hansen-Koharcheck, A. Espinoza, *Mars: The Pristine Beauty of the Red Planet* (University of Arizona Press, Tucson, 2017a)

A. McEwen, F. Rocard, X. Barral, *Mars: Une exploration photographique* (Editions Xavier Barral, Paris, 2017b)

Q. Meng, H. Wang, W. Wang et al., Desensitization design method of unobscured three-mirror anastigmatic optical systems with an adjustment-optimization-evaluation process. Appl. Opt. **57**(6), 1472–1481 (2018)

S. Murchie, R. Arvidson, P. Bedini et al., Compact Reconnaissance Imaging Spectrometer for Mars (CRISM) on Mars Reconnaissance Orbiter (MRO). J. Geophys. Res., Planets **112**, E05S03 (2007)